OBSERVATIONS AND MODELING OF THE EMERGING EXTREME-ULTRAVIOLET LOOPS IN THE QUIET SUN AS SEEN WITH THE *SOLAR DYNAMICS OBSERVATORY*

L. P. CHITTA[1,2], R. KARIYAPPA[2], A. A. VAN BALLEGOOIJEN[1], E. E. DELUCA[1], S. S. HASAN[2], AND A. HANSLMEIER[3]

[1] Harvard-Smithsonian Center for Astrophysics, 60 Garden Street, MS-15, Cambridge, MA 02138, USA
[2] Indian Institute of Astrophysics, Bangalore 560 034, India
[3] Institut für Physik, IGAM, Universität Graz, Universitätsplatz 5, A-8010 Graz, Austria

ABSTRACT

We used data from the Helioseismic and Magnetic Imager (HMI) and the Atmospheric Imaging Assembly (AIA) on the *Solar Dynamics Observatory* (*SDO*) to study coronal loops at small scales, emerging in the quiet Sun. With HMI line-of-sight magnetograms, we derive the integrated and unsigned photospheric magnetic flux at the loop footpoints in the photosphere. These loops are bright in the EUV channels of AIA. Using the six AIA EUV filters, we construct the differential emission measure (DEM) in the temperature range 5.7–6.5 in $\log T$ (K) for several hours of observations. The observed DEMs have a peak distribution around $\log T \approx 6.3$, falling rapidly at higher temperatures. For $\log T < 6.3$, DEMs are comparable to their peak values within an order of magnitude. The emission-weighted temperature is calculated, and its time variations are compared with those of magnetic flux. We present two possibilities for explaining the observed DEMs and temperatures variations. (1) Assuming that the observed loops are composed of a hundred thin strands with certain radius and length, we tested three time-dependent heating models and compared the resulting DEMs and temperatures with the observed quantities. This modeling used enthalpy-based thermal evolution of loops (EBTEL), a zero-dimensional (0D) hydrodynamic code. The comparisons suggest that a medium-frequency heating model with a population of different heating amplitudes can roughly reproduce the observations. (2) We also consider a loop model with steady heating and non-uniform cross-section of the loop along its length, and find that this model can also reproduce the observed DEMs, provided the loop expansion factor $\gamma \sim 5$–10. More observational constraints are required to better understand the nature of coronal heating in the short emerging loops on the quiet Sun.

Key words: Sun: atmosphere – Sun: corona – Sun: photosphere – Sun: surface magnetism

Online-only material: animation, color figures

1. INTRODUCTION

A part of the magnetic field originating in the photospheric sub-surface layers reaches higher up in the solar atmosphere and forms loop-like structures, the building blocks of the solar corona. These loops harbor plasma, which is heated up to a few million kelvin, much higher than the photospheric temperature. Finding the source and nature of the energy required to heat the corona along with the process of heating is one of the most sought-after questions in the field of astrophysics (for reviews on coronal heating, see, for example, Zirker 1993; Narain & Ulmschneider 1996; Klimchuk 2006; Reale 2010). Studying the dynamics of the plasma-filled loops is important to understand the heating mechanisms responsible for these high temperatures. Observational, theoretical, and numerical advances have been made over several decades to understand the physics involved in these processes. Some of the early works on this subject include the ideas of damping of magnetohydrodynamic waves in the lower corona to heat the solar atmosphere (Alfvén 1947; for a recent review on waves in the solar corona, see Nakariakov & Verwichte 2005).

From the early X-ray observations (Vaiana et al. 1973), it became evident that the solar corona is confined in the form of loops outlined by the underlying photospheric magnetic field. Later, Rosner et al. (1978) gave an analytical model for the quiescent coronal loops, assuming that these structures are in hydrostatic equilibrium. They suggested that the observations are indicative of a steady-state heating process. Parker (1988), Cargill (1994), and Cargill & Klimchuk (1997) put forward the idea of intermittent and impulsive (nanoflare) heating as a viable mechanism. It is now generally believed, and widely accepted, that the magnetic field plays an important role in generating and transporting the energy required to maintain the temperatures of the corona. It remains unclear and difficult to identify the dominant process responsible for heating of the solar atmosphere.

As the diagnostics of tenuous coronal plasma improved with the advent of high spatial and temporal resolution space-based instruments, an alternative but relevant debate emerged within the community, namely, the frequency of required heating events. The plasma filling the loops responds to the impulse of heating, and this depends on whether the plasma is reheated before it is completely cooled down (high-frequency model—steady heating) or not (low-frequency model—nanoflares). Should either of these models operate, they predict certain physical properties of the loops, which can be compared with the observations (see Reale 2010 for a broad review on coronal loop observations and modeling).

With a wide range of field strengths and sizes of magnetic elements, coronal loops also have wide temperature and length distributions. Usually, the loops are classified as "hot" ($T > 2$–3 MK) and "warm" ($T \approx 1$–2 MK) depending on their temperature regime. Both steady and impulsive heating models have been extensively used to explain the observed temperatures, loop intensity structure, etc. Studies indicate that the hot plasma is consistent with both steady heating models (Warren et al. 2010; Winebarger et al. 2011) and impulsive heating models (Tripathi et al. 2010; Viall & Klimchuk 2012).

The warm loops are found to be continuously evolving and not in equilibrium (see, for example, Ugarte-Urra et al. 2009), and their properties are well explained by impulsive heating models (Spadaro et al. 2003). It is also suggested that the age of an active region might play an important role in determining the dominance of one process over the other (Schmelz & Pathak 2012; Ugarte-Urra & Warren 2012).

The active regions are well studied both in terms of observations and modeling. However, the situation is not so clear in the case of small loops in the quiet Sun. The classification of "hot" and "warm" loops may not be relevant in these features, owing to their compact magnetic structure and narrow temperature range compared to the active regions. These short loops are connected to magnetic bipoles in the photosphere. Their origin can be traced to either flux emergence or convergence of opposite polarities with reconnection. The magnetic fluxes associated with these regions are typically in the range of 10^{19}–10^{20} Mx. The electron number density in such loops measured using density sensitive lines is in the order of 10^9 cm^{-3} (Ugarte-Urra et al. 2005; Pérez-Suárez et al. 2008; Doschek et al. 2010).

In this study, we are primarily interested in understanding the nature of the heating that produces the observed 1–2 MK temperature in these small bipoles, in particular the frequency of heating events. Also, to better understand the relation between photospheric magnetic field and the coronal loop temperatures, we chose to study emerging flux events. In these events it is easy to identify the loops and their footpoints in the photosphere. We follow their formation and evolution over many hours. In the following section, we present the observational results. Section 3 describes the loop modeling and the simple heating models we tested in this work. Finally, we summarize the results and discuss some relevant aspects that require further investigation.

2. OBSERVATIONAL RESULTS

In this section we give a brief note on the data sets used and present the results derived, namely, the photospheric magnetic flux and coronal temperatures. The line-of-sight magnetograms observed with the Helioseismic and Magnetic Imager (HMI; Scherrer et al. 2012; Schou et al. 2012) and the intensity images from the EUV channels of the Atmospheric Imaging Assembly (AIA; Lemen et al. 2012) are used. HMI and AIA are two of the three instruments on board the *Solar Dynamics Observatory* (*SDO*; Pesnell et al. 2012). Data are taken from 2011 February 10 and 2012 March 17 observations, spanning about 12 hr each. *SDO* observes the full disk of the Sun continuously in different filters with a high cadence of 12 s. We selected a region near disk center with the criteria that we see emerging magnetic field and coronal loops close to the beginning of the selected time sequence. A few cases of evolved bipoles are also considered.

AIA data contain time sequences from 94 Å, 131 Å, 171 Å, 193 Å, 211 Å, and 335 Å EUV channels. Data are processed with standard procedures available in the *solarsoft* library. Alignment between the data from all these channels is crucial. Using 171 Å images as reference, and a cross-correlation technique, we aligned all data to within a pixel. The emerging bipoles are identified both in HMI and AIA. The tracked data cubes of such bipoles are extracted for further analysis. To enhance the signal-to-noise ratio, we prepare the 12 s cadence AIA data to 1 minute cadence by averaging five exposures in each channel. Next, to derive the physical properties of the plasma, we adopt the differential emission measure (DEM), which is related to the electron number density (n_e) and the line-of-sight plasma
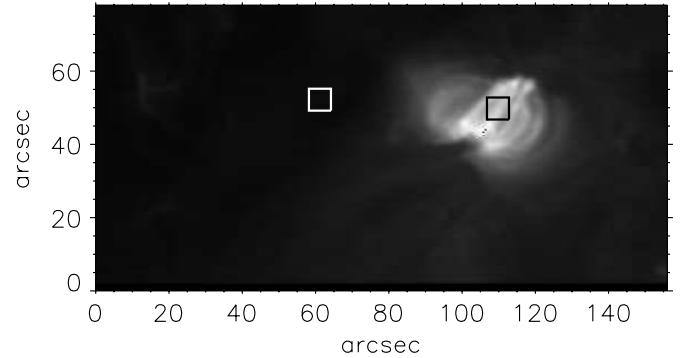

Figure 1. Context image showing one of the analyzed bipoles as seen in the AIA 193 Å channel. The regions marked with black (near loop top) and white (background region) boxes are used for further analysis to produce DEMs (see Figure 2(a)).

temperature gradient, and is defined as

$$\varphi(T) = n_e^2 \frac{dh}{dT}. \tag{1}$$

We use data from six AIA EUV channels, along with the filter responses[4] as input to construct DEM(T) (cm^{-5} K^{-1}), at each pixel, using `xrt_dem_iterative2.pro` (Golub et al. 2004; Weber et al. 2004, distributed in *solarsoft*). In this program, an initial DEM is guessed and folded through the filter responses to generate model observations, which are iteratively used to reduce the χ^2 between the original and modeled observations. This program uses a much tested IDL routine `mpfit.pro` (Markwardt 2009) that performs a Levenberg–Marquardt technique to solve the least-squares problem.

We show results from four emerging bipoles in this work. In Figure 1, we plot the region of interest for one of the bipoles analyzed, as seen in AIA 193 Å. The image saturates at 750 DN s^{-1}. For these bipoles, a series of DEMs are constructed near the loop top (for example, from a region within the black box shown in Figure 1) at each pixel in a $6'' \times 6''$ region, over several hours of observations. The predicted intensities from forward modeling of the derived DEMs match the observed intensities within the limits of errors. Since we restrict the DEMs within a limited range of temperature, the predicted intensities will be lower limits of the observed values. In Figure 2, we plot the average emission from this area as a function of temperature ($\log T$) for all times. Each panel corresponds to a bipole. The dots denote the time dependence. At any given temperature, to show the emission distribution in time, we gave a small offset to DEMs in temperature (and that is the reason we see a small spread of DEMs along $\log T$). Additionally, the temporal distributions also give a sense for the errors in the DEMs. The solid lines are respective temporal medians for all DEMs. They have a peak close to $\log T$ (K) of 6.2–6.3. At higher T, they show a rapid decline and also the DEMs are not well constrained. On the other hand, at lower T, the emission stays comparable to the peak emission. Similar results were obtained using *Hinode*/EIS observations, but for a coronal hole bright point (cf. Figure 12, Doschek et al. 2010).

We also note that there is no background subtraction to the data in the DEM analysis. The small loop structures we

---

[4] The filter responses of 94 and 131 Å channels are empirically modified to include contributions from Fe IX and Fe XII for 94 Å, and from Fe VIII and Fe XI for 131 Å. The revised response functions can be obtained using `aia_get_response` with a keyword `chiantifix` available in *solarsoft*.
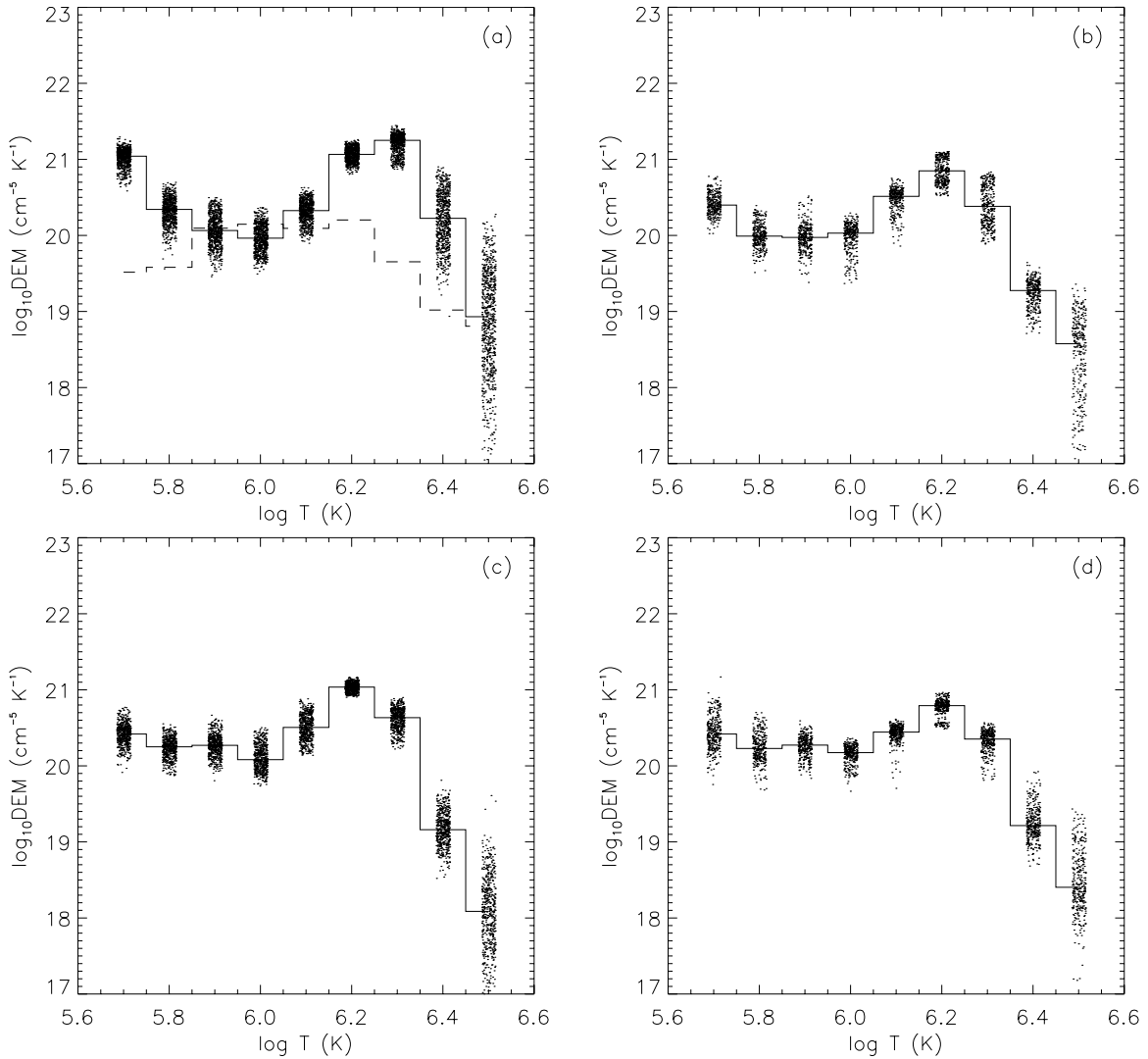
Figure 2. DEMs of four bipoles obtained from the observations plotted as a function of temperature for all times (dots). A small offset in temperature is given to the DEMs to show the temporal distribution. The solid line is the temporal median of DEMs obtained for the respective cases. Observed DEMs have a peak around log T of 6.2–6.3. The dashed histogram in panel (a) is the temporal median of five DEMs, at random times, obtained from a *background* region close to the corresponding bipole.

analyzed have their loop apex and footpoints in the same plane along the line of sight; much of the emission contribution may be primarily dominated by the loop apex with a part of it originating from the footpoints. To compare the background contribution to the resulting DEMs, for example panel (a) in Figure 2, we considered a 10 × 10 pixel *background* region adjacent to that bipole (marked with a white box in Figure 1). The DEMs are constructed for this region at five random times, and the temporal median is plotted as a dashed histogram in Figure 2(a). This shows that the observed DEM lies well above the background, not only for log T in the range 6.2–6.4 but also at low temperatures (log $T \leqslant 5.8$). The small scatter in the DEM at low T suggests that this emission is real and is not an artifact of the DEM inversion. The DEMs are now used to derive an emission-weighted temperature (T_{DEM}) using the relation

$$T_{\mathrm{DEM}} = \frac{\Sigma\{\mathrm{DEM}(T_i)T_i\Delta T_i\}}{\Sigma\{\mathrm{DEM}(T_i)\Delta T_i\}}, \quad (2)$$

where $\Delta T_i = 0.1$ in log (T) is the width of the temperature bin around T_i. The time variations of T_{DEM} will be used later for comparison with loop models.

Integrated unsigned magnetic flux of both polarities associated with these examples, as a function of time, is also calculated from HMI.[5] Such profiles of temperature and magnetic field for a sample of four bipoles are plotted in Figure 3. Three cases of newly emerging bipoles (panels (a), (b), and (d)) and a case of an emerged bipole (panel (c)) are shown. The black curves are time profiles of magnetic flux (10^{19}–10^{20} Mx), and red curves are temperatures in the range of 1–2 MK.

Though they all fall in a category of emerging/emerged loops, there is no clear relation between the magnetic flux at the photosphere and the coronal loop temperature. In other words, it is not trivial to directly relate the field changes in the photosphere to the temperature fluctuations in the corona. For example in Figure 3(a), there is a strong correlation between the two physical quantities in the long-term trend, but in panel (b) the temperature seems to increase while the flux decreases. In panels (c) and (d), it is more complicated. We suggest that every emerging bipole may behave differently

---

[5] The two polarities are separated by a distance of approximately 10–15 Mm in the photosphere.
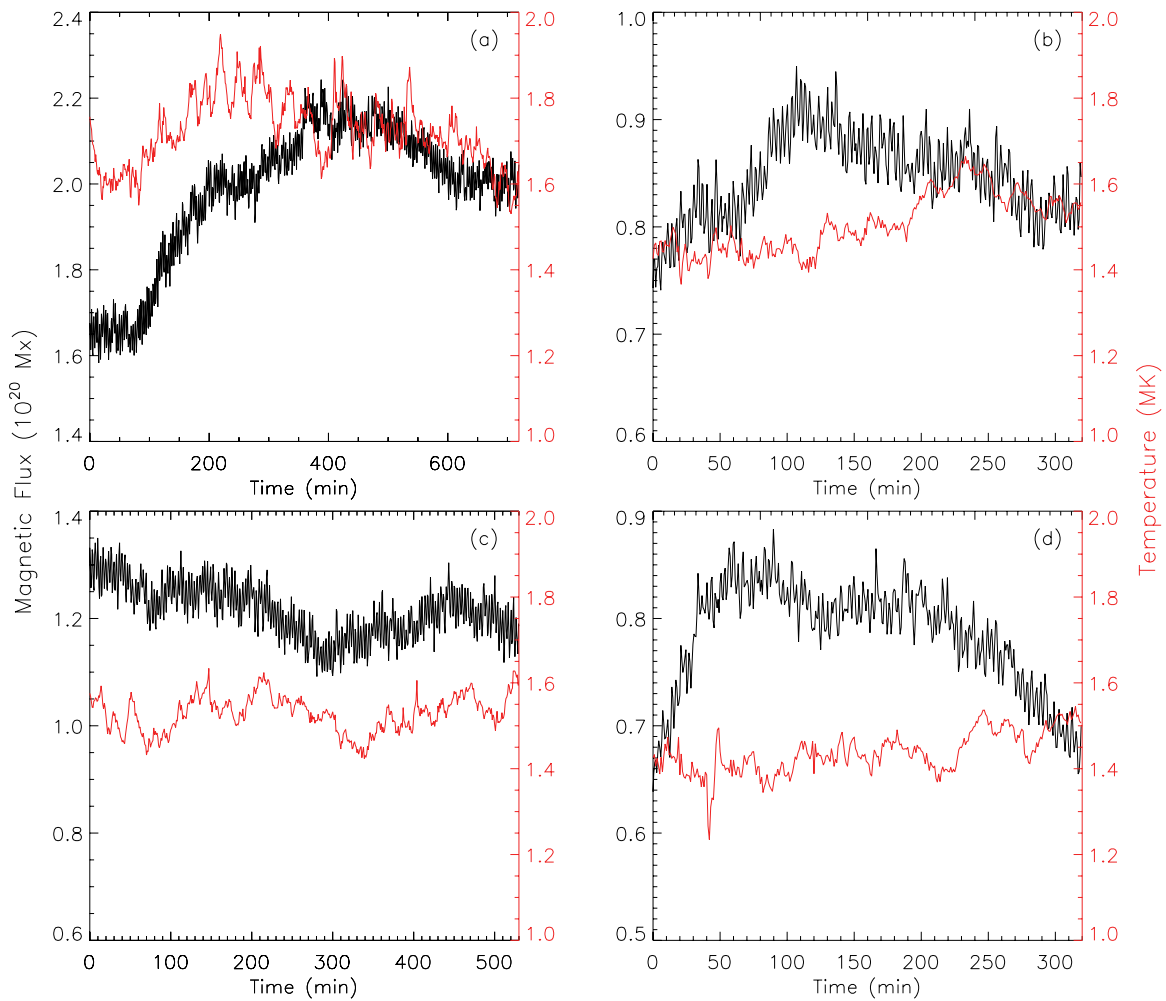
Figure 3. Magnetic flux and loop temperatures for a sample of four bipoles. The black curves (left axes) correspond to the integrated photospheric flux density of the bipoles. The red curves (right axes) are the emission-weighted and averaged coronal temperature profiles for the respective bipoles. Panels (a), (b), and (d) are for emerging bipoles, and panel (c) is for an evolved bipole.

(A color version of this figure is available in the online journal.)

owing to its surrounding structures both in the corona and photosphere. However, a common signature is that the temperature fluctuates/rises at some stage in the emergence process.

To further illustrate this behavior, we consider another example of an emerged bipole. In Figure 4, we plot the magnetic flux (black curve) and temperatures (red curves) of this bipole. A sample image of this example from a particular time is also shown above (magnetic structure) and below (coronal loop) the plot. The thin vertical line demarcates the time of snapshot. The solid and dashed red curves are average temperatures derived from two adjacent regions (marked with solid and dashed lines in the image below the plot) of $2\rlap{.}{''}4 \times 15''$ size each. In the accompanying animation, it is observed that the drop in temperature after 500 minutes is due to the reconnection (in the corona) of the parent bipole with the adjacent opposite polarity regions, changing the topology of the field and completely disrupting the main loop. Hence, the observed temperature of the loops originating from small ephemeral regions possibly depends on various factors.

3. LOOP MODELING

The temperature profile of the loop is a good diagnostic for the loop dynamics, but to get a better picture we also need to estimate

the heating rate required to produce the observed temperatures. To this end, we use enthalpy-based thermal evolution of loops (EBTEL; Klimchuk et al. 2008; Cargill et al. 2012). EBTEL is a time-dependent zero-dimensional (0D), hydrodynamic coronal loop model. For a given loop half-length and volumetric heating rate, the code returns the loop properties in terms of average temperature, density, and pressure of the loop and also the values of these quantities at the loop apex (see Appendix A).

We use EBTEL to model and derive the properties similar to the observed loops (we consider the example shown in Figure 3(a) for this purpose). The properties include the DEM as a function of temperature and the emission-weighted temperature. We compare three different heating scenarios and discuss the results. For the models presented in the next three subsections, we make the following assumptions: (1) a loop is composed of a hundred individual strands, each with a constant length[6] of about 18 Mm and a uniform radius of about 0.1 Mm. In Figure 5, we plot the length and radius of a single strand as a function of time (thick solid and dashed lines, respectively). (2) Each strand is randomly heated with a certain heating profile over a period of 500 minutes. (3) The average values of various

---

[6] This is only a rough estimate of the length based on the footpoint separation in the photosphere.
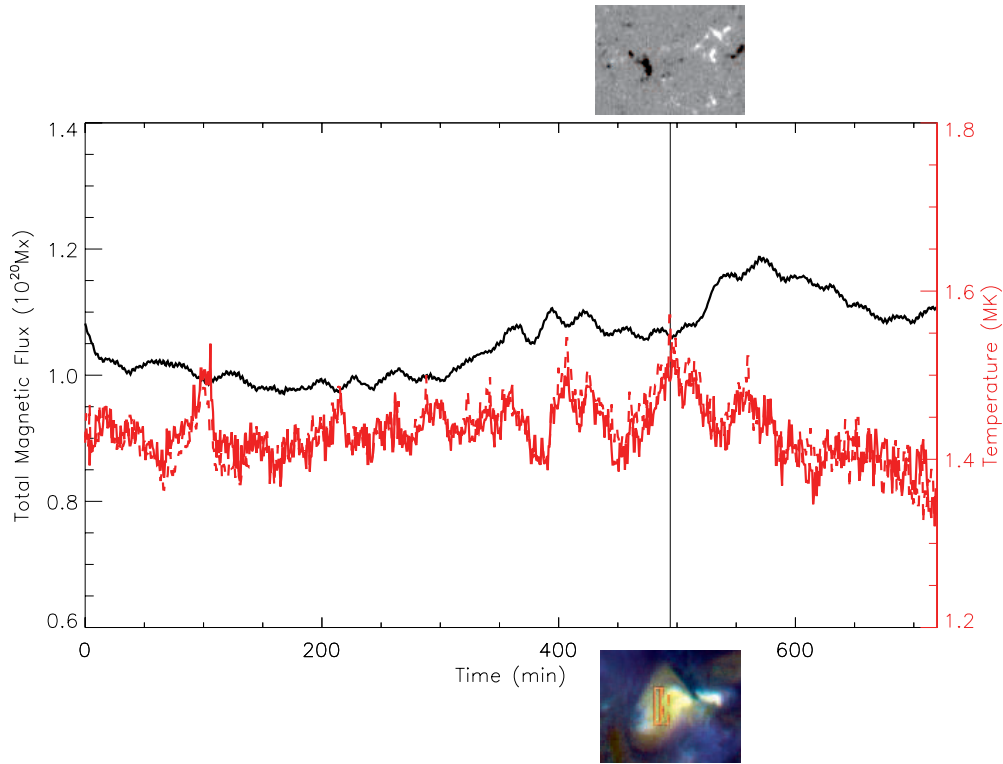
Figure 4. Same as in Figure 3. Integrated flux density (black curve) and the temperatures (red solid and dashed curves) of an evolved bipole are plotted. A snapshot of the photospheric field configuration (top image, from HMI, $53'' \times 39''$) and the corresponding coronal loop structure (bottom composite image, from AIA 171 Å, 193 Å, 211 Å channels, $60'' \times 48''$) are shown for a particular time as demarcated by the thin vertical line. The solid and dashed red curves are the emission-weighted temperatures derived from 4×25 pixel ($2''.4 \times 15''$) rectangular boxes, from the regions marked in the bottom image. A complete observed evolution of this example is presented as an animation, accompanying this figure.

(An animation and a color version of this figure are available in the online journal.)
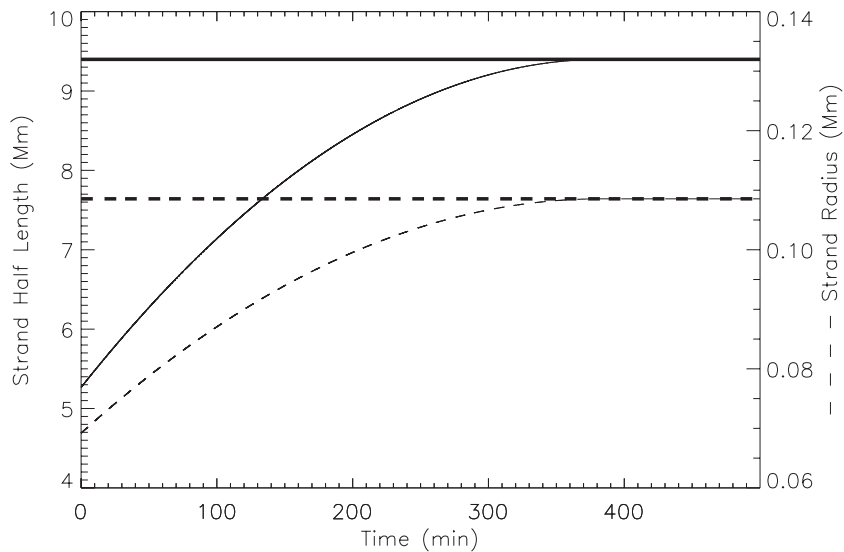

Figure 5. Physical dimensions of the strands used in this study. Thick solid and dashed lines, respectively, are the half-length and radius of a constant strand. Thin solid and dashed curves, respectively, are the half-length and radius of an expanding strand.

physical quantities over all the strands represent the properties of the whole loop. Along with these assumptions, the heating events are chosen such that the modeled emission-weighted temperatures closely match the observed temperatures.

In Section 3.1, we describe the medium-frequency heating model. Section 3.2 deals with the low-frequency heating model. A medium-frequency hybrid heating model is discussed in Sections 3.3 and 3.4. In Section 3.5, we present an alternative explanation for the observed DEMs by considering a non-uniform cross-section of the loop.

3.1. Medium-frequency Heating Model

In the medium-frequency heating model (case 1), individual strands are randomly heated with heating rates having 50–100 s temporal fluctuations. These rates are generated by a sequence
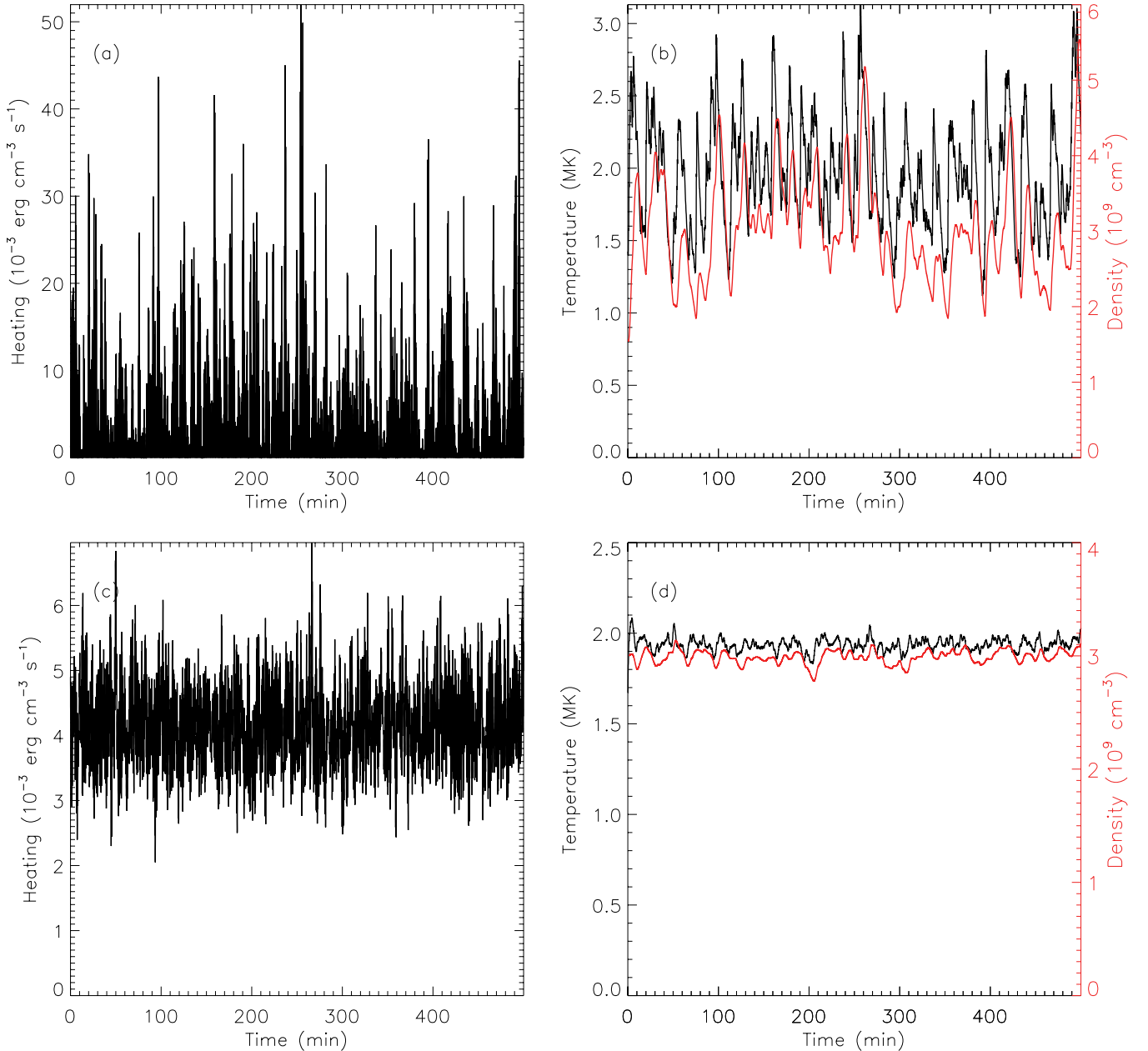
Figure 6. Results from a medium-frequency heating model (case 1). All the hundred strands are heated with approximately the same average heating rate. (a) A representative input heating given to a single strand with temporal fluctuations of 50–100 s. The base heating rate is 10^{-6} erg cm^{-3} s^{-1} for all the strands. The amplitudes of the heating rate fluctuate up to four orders of magnitude. (b) The resulting temperature of the strand apex (black, left axis) and loop density (red, right axis) for the heating profile shown in panel (a). (c) The average heating rate of a hundred random realizations. (d) The average loop apex temperature (black, left axis) and the average loop density (red, right axis) averaged over a hundred strands, representing an observed loop.

(A color version of this figure is available in the online journal.)

of random numbers, and further filtering the signal within the desired band of periods. The base or minimum heating rate is 10^{-6} erg cm^{-3} s^{-1}, and the amplitude of the fluctuations varies by up to four orders of magnitude. The average heating rate for a single strand over the entire duration of 500 minutes is about 4×10^{-3} erg cm^{-3} s^{-1}.

A representative heating rate for one of the strands is plotted in Figure 6(a). The plasma is reheated continuously before it is cooled to the equilibrium temperature due to base heating. In panel (b), we plot the resulting temperature of the strand apex (black, left axis) along with the resulting strand density (red, right axis). The temperature variations are 1–3 MK within in a single strand. Panel (c) is the average heating rate of

all strands as a function of time. It should be noted that the frequency of this average quantity is not a relevant factor in distinguishing between various heating cases. Similarly, in panel (d) we plot the average loop apex temperature (black, left axis) and the average loop density (red, right axis). Since the observed temperatures are derived from weighting the emission distribution, the temperature of the loop apex in panel (d) cannot be directly compared with its observed counterpart.

In the top panel of Figure 7, we plot the observed DEMs (black dots). The observed DEMs have a broad distribution in temperature with a peak at log T of 6.3 and another peak at log T of 5.7 (same as Figure 2(a)). The modeled DEMs, which have a narrow distribution, are plotted as red dots with
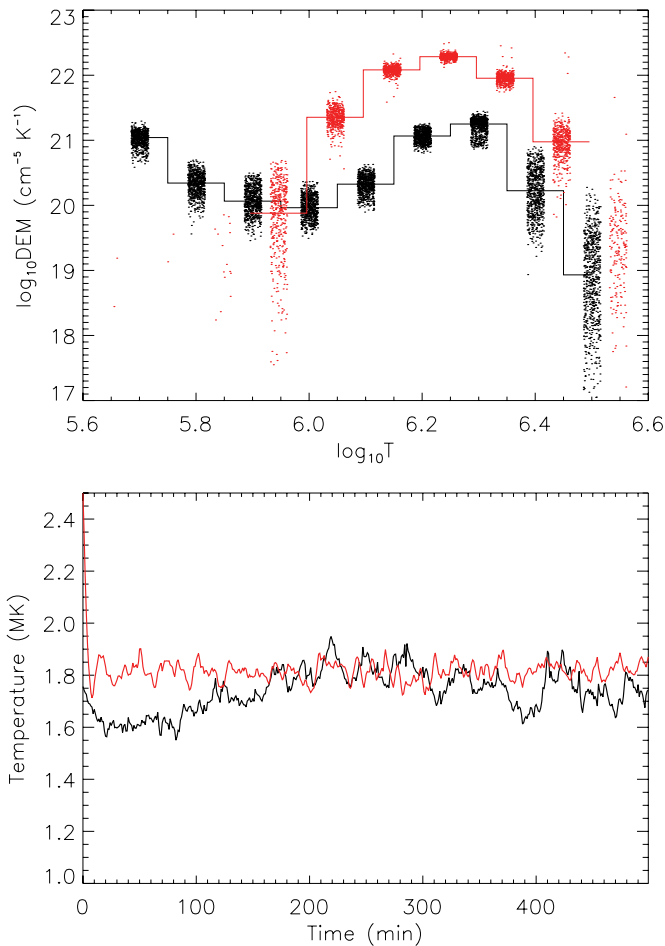
Figure 7. Comparison of DEM results obtained for case 1 with the observations. Top panel: DEMs from observations (black dots) and the modeled DEMs (red dots) are shown. All DEMs are given small temperature offsets for a better visualization of the distributions. The black and red solid lines are the temporal medians of the observed and modeled DEMs, respectively. Bottom panel: emission-weighted temperature derived from observations (black) and modeling (red).

(A color version of this figure is available in the online journal.)

a similar temperature offset. Since there are heating events occurring almost continuously compared to the cooling time of the strands, the loop has no time to cool down completely and the temperature stays steady, with small fluctuations. Because of this reason, all the emission comes from a narrow distribution of temperatures, which is reflected in the modeled results.

The bottom panel is the resulting emission-weighted temperatures from observations (black) and modeling (red). Note that the range and level of fluctuations in the temperature match very well, but the modeled DEM has a peak at $\log T$ of 6.25, and the predicted emission about this temperature is at least an order of magnitude greater than the observed values. Further, the model predicts a weak or no emission at lower T. By increasing the magnitude of the heating rate to match the temperature at which the peak emission occurs, it will inherently increase the emission and also the weighted temperature well beyond the observed T.

3.2. Low-frequency Heating Model

In the low-frequency heating model (case 2), each strand is impulsively heated five times with an average interval of 100 minutes between impulses. Each triangular pulse has a

width of 500 s and a peak input of 10^{-2} erg cm^{-3} s^{-1}. Further, the base heating remains the same as in case 1. In Figure 8(a), we plot a sample profile of heat input given to one of the strands. Panel (b) shows the resulting temperature and density. Note that once the temperature reaches a maximum value, it takes about 70 minutes for the strand to completely cool down.

The average heating rate in panel (c) is less by a factor of five than that of case 1. It can be seen that the temperature (panel (b)) in this model has a broad distribution, which is reflected in a very broad DEM distribution shown in Figure 9 (top panel, red). At $\log T$ of 6.5 the model produces a well-constrained DEM that is higher than the observed DEM, although the observations are less constrained at those temperatures. Also, the model predicts an overall higher emission at $\log(T) \approx 6.0$.

The predicted emission-weighted temperature (bottom panel, red) is comparable with the observed temperature (bottom panel, black). The level of fluctuations and the short-term trend in the red curve are higher than what is seen in the observations. Furthermore, if the number of heating events is fewer than what is considered here (five), but with stronger impulses, the fluctuations now become noticeably large and the observations should reveal these features.

3.3. Medium-frequency Hybrid Heating Model

For cases 1 and 2 we adjusted the model parameters such that the DEM-weighted temperature (T_{DEM}) roughly matches the observed temperature for region 1. However, we find that the overall structure and features of the predicted DEM(T) do not match the DEM(T) derived from AIA observations. Therefore, neither of these models is fruitful in describing the 1–2 MK emerging loops in the quiet Sun. We suggest that the heating events may have a broad range and/or a population of different heating amplitudes, influencing different strands.

From the observational point of view, each strand in the loop is dynamically evolving and the lifetime of this unit is not clearly known. New strands emerge with the photospheric flux and replace the older ones in the loop. To investigate this problem further, a hybrid heating model (case 3) has been considered. In this model, we start with a simple assumption that 20% of the strands are rapidly heated with an excess amount of the average heating rate of 50 times greater than the remaining 80% of the strands. All strands receive a base heating similar to that of cases 1 and 2.

In Figure 10, we plot the heating rates, temperature, and densities and also the respective average quantities. The profile in panel (a) is a low-amplitude heating for a strand in the 80% population. The profiles shown in panel (b) are similar to those of Figure 6(b), except for the overall lower values. Panels (c) and (d) show results averaged over all the strands, including the 20% that receive a higher level of heating. In Figure 11, we show the DEM results for this case. The top panel is for the observed (black) and predicted (red) DEMs. We see that the predicted DEMs now have two distributions, clearly originating from the two populations of heating events. It is interesting to note how closely the observed and predicted DEMs match. The emission-weighted temperature is shown in the bottom panel of Figure 11. The fairly well-reproduced quantities from this model suggest that a coronal loop, which has a bundle of many strands, can be heated by considering different amplitudes of medium-frequency heating events. This is certainly a plausible assumption, because these emerging bipoles evolve continuously and various reasons can contribute to different heating episodes.
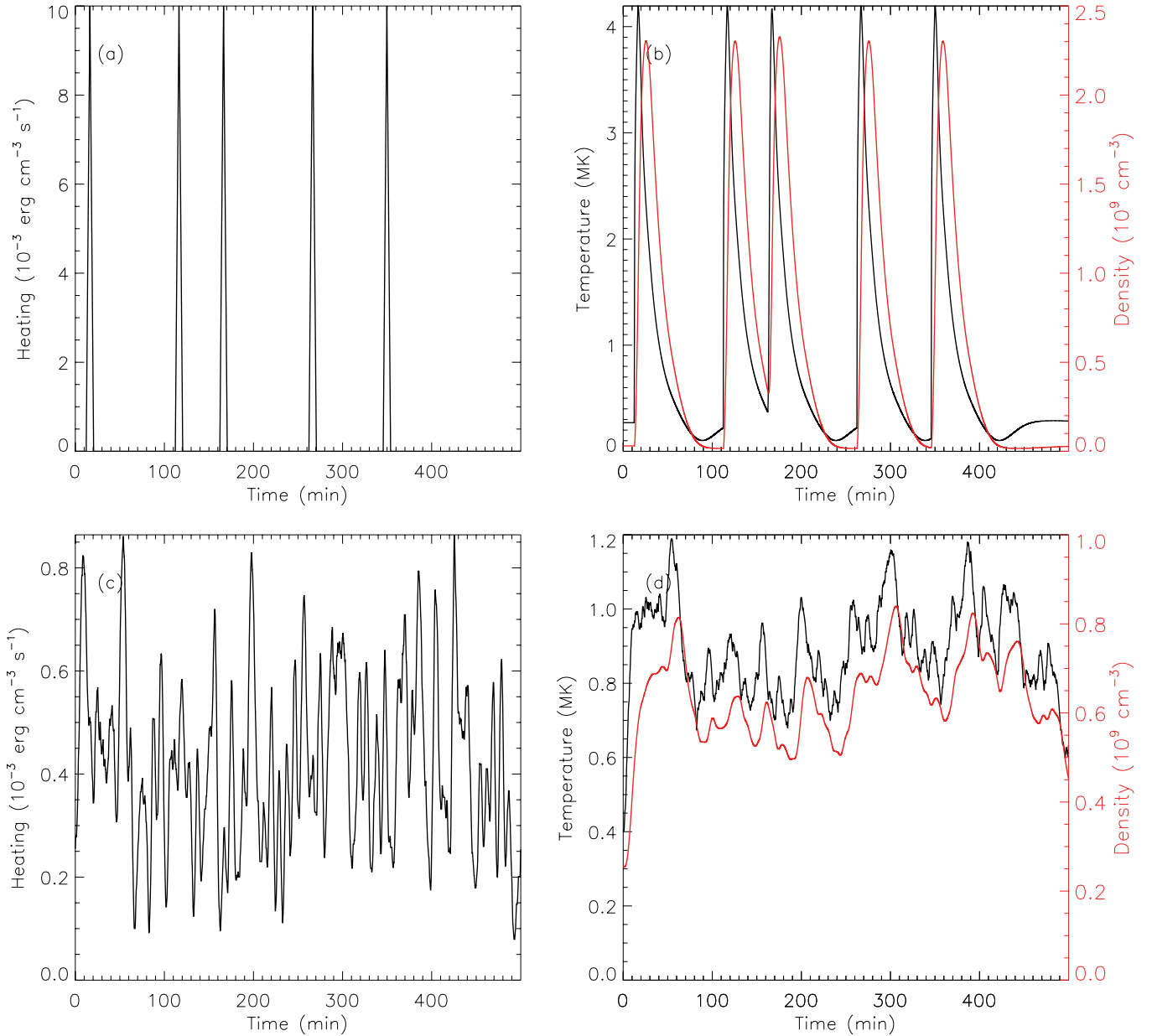
Figure 8. Same as Figure 6. Results from a low-frequency (impulsive) heating model (case 2). On average, each strand is heated once every 6000 s, with a triangular heating pulse having a maximum of 10^{-2} erg cm^{-3} s^{-1} and a width of 500 s.
(A color version of this figure is available in the online journal.)

Alternatively, we can also assume that each strand spends 20% of its time being heated to higher values (similar to the 20% strands case described previously), and the remaining time to lower values. Both the scenarios produce similar results. In Figure 12, we plot the results from this alternative case. Panel (a) is a sample heating profile showing both low and high heating events. In panel (b) the loop apex temperature and density are shown. In panel (c), the observed (black) and predicted (red) DEMs are plotted along with their respective temporal medians.

3.4. A Case of Expanding Loop

In general, the coronal loop length increases with time as it emerges through the solar atmosphere. Also, as the strength of the magnetic field drops with height, the area of strand increases with time. Due to this expansion, infilling plasma may experience additional adiabatic cooling effects, as the loop pressure and density are modified by the volume change (see

Appendix A). We tested the heating model described in case 3 on a slowly expanding loop, comprising a hundred strands as explained in the previous sections.

The half-length and radius of a single strand are shown as thin solid and dashed curves in Figure 5. The DEMs and T are plotted in Figure 13. The way we consider the volume expansion is that each strand slowly expands for about 350 minutes and then the expansion saturates to a constant value. This constant value matches with the length and radius of the strand chosen in all the cases. It is observed that for a slowly expanding loop the adiabatic cooling effect can be negligible. There are two competing effects here. Under equilibrium conditions, the temperature of the loop increases with the length. In our slowly expanding loop, the cooling is compensated for with the length increase. But in reality, the rate of volume expansion can be entirely different and more rapid than what we considered here. These effects become important when changes in the loop
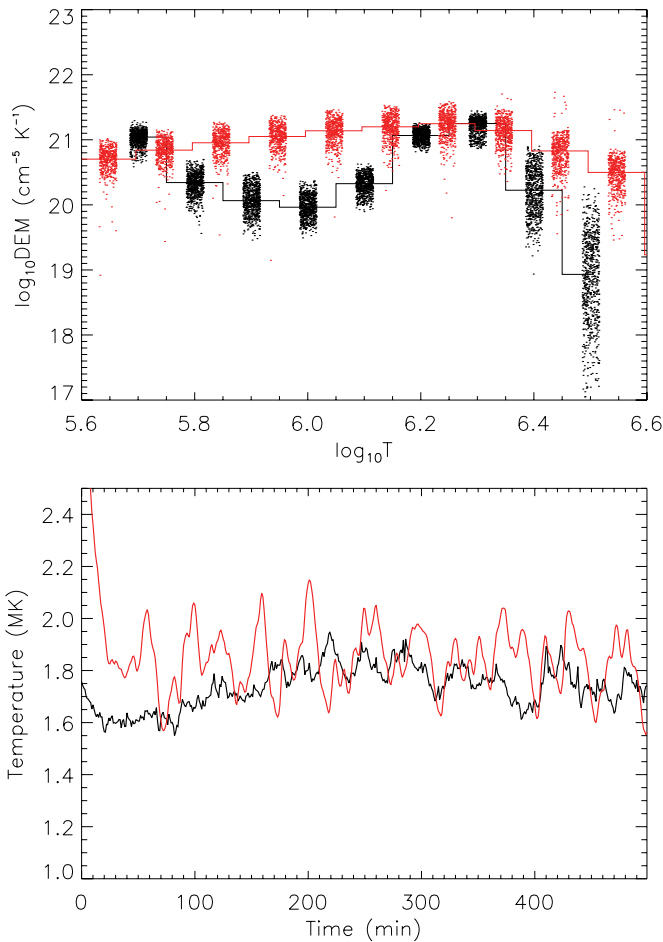
Figure 9. Same as Figure 7, but obtained for case 2.
(A color version of this figure is available in the online journal.)

pressure and density due to expansion alone and heating are comparable.

3.5. Effects of Non-uniform Cross-section of the Loop

In the above EBTEL-based models, the emission is assumed to come from the coronal portion of the loop. EBTEL also predicts the emission from the transition region (TR) to model the lower temperatures. However, the predicted TR emission is strong and rather flat relative to the corona. Inclusion of up to 5%–10% of the TR emission will not affect the results, but adding more contribution from the TR requires stronger heating to match the observed emission-weighted temperature. This results in a strong emission from the higher temperature, which is not observed.

One possible reason for the strong TR DEMs produced by EBTEL is that the model assumes a constant cross-section over the length of the loop, whereas the loops on the Sun have significant expansion factors (γ) between the loop footpoints in the TR and the loop top in the corona. Potential field modeling of active regions (e.g., Asgari-Targhi & van Ballegooijen 2012) indicates $\gamma = 3$–30, depending on height, and similar expansion factors may occur on the quiet Sun. When the cross-sectional area A of a loop increases with height, the volume of plasma at coronal temperatures is increased relative to that at TR temperatures, so the slope of the DEM(T) curve becomes steeper and more consistent with observations.

To demonstrate this effect, we developed a simple loop model for the case that the cross-section A varies along the loop. The heating is assumed to be steady in time. The model is described in Appendix B. It allows us to compute the DEM(T) for a single loop with a given expansion factor γ, half-length L, and peak temperature $T_{\max}$ (we use $L = 9$ Mm). We repeat the calculation for different peak temperatures ($6.0 < \log_{10} T_{\max} < 6.4$) and compute the average DEM(T). In Figure 14, we plot the DEM results for $\gamma = 1$ (left panel) and $\gamma = 5$ (right panel). Note that for a loop with uniform cross-section ($\gamma = 1$), DEM(T) is flat for $T > 10^5$ K, similar to the DEMs predicted with the EBTEL code (see Klimchuk et al. 2008). In contrast, for $\gamma = 5$ the peak value of the DEM in the corona is about eight times its value in the TR, similar to the observed DEMs (see Figure 2). These results suggest that the overall shape of the observed DEM can be very well reproduced with a collection of hot loops ($T_{\max} > 1$ MK) that have significant expansion factors ($\gamma \sim$ 5–10). However, the peak value of the DEM as predicted by the model is larger than the observed value by a factor of about 100. Therefore, the loops must fill only a small fraction of the coronal volume (filling factor $\sim$1%).

4. SUMMARY AND DISCUSSION

Using the high temporal cadence observations from the HMI and AIA instruments on board *SDO*, we studied the cases of emerging bipolar regions in the quiet Sun. High-cadence data from AIA including six EUV channels are re-sampled to 1 minute data to improve the signal-to-noise ratio as well as to have a good temporal resolution. Further, `xrt_dem_iterative2.pro` is used to construct DEMs near the loop top in a $6'' \times 6''$ pixel region (Section 2, Figure 2). From these DEMs, we get the temporal evolution of emission-weighted temperature with Equation (2).

Integrated unsigned magnetic flux derived from the HMI observations (10^{19}–10^{20} Mx) is compared with the temperature of the loop for a sample of four bipoles (Figure 3). There is no clear relation between the two quantities, suggesting that for these small emerging bipoles, the surrounding regions in the photosphere and higher atmosphere play an important role in the loop evolution.

To estimate the energetics involved in the formation of these loops, we use a hydrodynamic loop model (EBTEL) to simulate the DEMs and emission-weighted temperatures. We assume that a loop is a bundle of 100 strands, each having a length of about 18 Mm and a uniform radius of 0.1 Mm. Furthermore, each strand is randomly heated and the average effect describes the properties of the observed loop. To this end, we tested three simple heating events with varied heating frequencies as described in Sections 3.1–3.4. The average heating input in our study ($\approx 10^6$ erg cm^{-2} s^{-1}) is in close agreement with the approximate energy losses observed in the quiet Sun. The 3σ values of the fluctuations in T_{DEM} (MK) are about 0.25, 0.16, 0.55, and 0.24 for the observations, cases 1, 2, and 3(a), respectively.

In case 3, we tested the following sub-cases: (a) 20% of the strands are heated to high heating values all the time, and the remaining strands are heated to low heating values (Section 3.3); (b) all strands are heated to high heating values 20% of their time (Section 3.3); and (c) same as case 3(a), but for expanding strands to account for the adiabatic cooling effects (Section 3.4). It is shown that cases 3(a) and (b) are equivalent and match the observations fairly well. This suggests that there may be a range of heating events operating in the loops at a given time. In cases 2
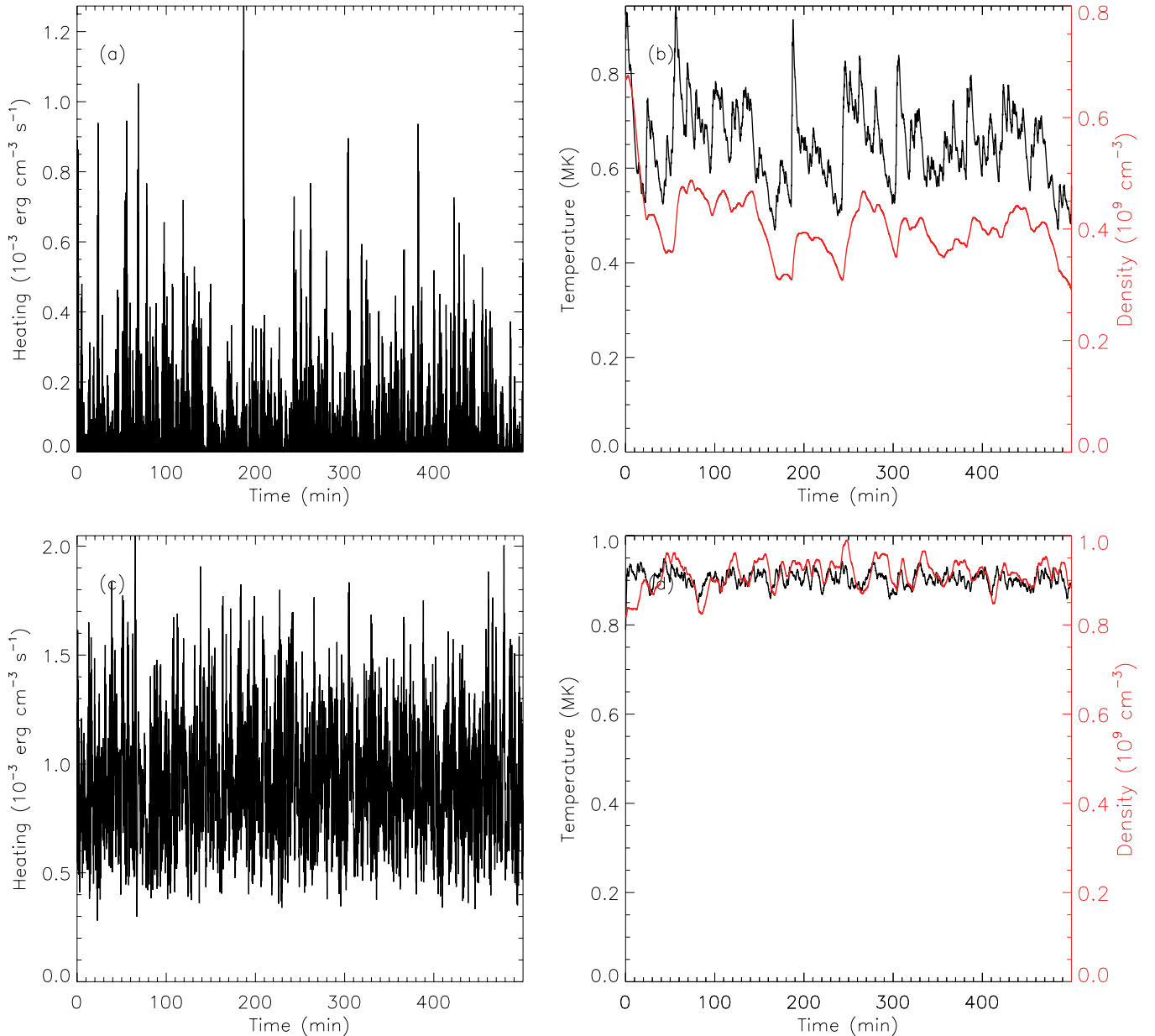
Figure 10. Same as Figure 6. Results from a medium-frequency hybrid heating model (case 3). Twenty percent of the strands are subjected to higher average heating inputs, but with same temporal fluctuations as in case 1 (see the text for details). Shown in panel (a) is an example of lower heating rate.
(A color version of this figure is available in the online journal.)

and 3(b), though there are only a few large heating events, the essential difference between the two cases is that, unlike in case 2, the duration of a single high heating phase in case 3(b) itself is longer than the typical plasma cooling time (making case 3(b) statistically a steady heating model). This allows case 3(b) to find a DEM peak at higher temperatures. The model described in case 3 is the best model we could obtain with the scope of the present work. Mixing low and medium heating in various proportions with different average heating rates shows discrepancy and does not fit the observations completely. These results are based on the assumption that the emitting plasma has coronal origin.

Alternatively, we also argued that to include TR emission in the model, it is important to consider an expansion of the loop from TR to corona. In this scenario, a steady heating model for loops with loop apex temperature $>10^6$ K can well reproduce the observed DEMs, assuming $\sim 1\%$ plasma filling factor.

The reliability of AIA DEMs is a matter of debate. O'Dwyer et al. (2010) studied the contribution of spectral lines and continuum emission to the AIA EUV channels using CHIANTI atomic database. They emphasize that the contribution of particular spectral lines and continuum emission can affect the interpretation of the observed features, when AIA channels are used to observe regions other than those for which the channels were designed. Del Zanna et al. (2011) compared AIA DEMs with the *Hinode*/EIS observations of active regions. They found discrepancies between the derived DEMs. This is mainly due to the multi-thermal nature of AIA response curves, which have contributions from cooler components. The cooler emission below 6.0 (in log T) seen in our observations could be due to the double-peaked nature of AIA responses as suggested by Del Zanna et al. (2011). Empirically modified filter response curves for AIA are derived to address some of these issues; however, the role of this possible contamination in an already cool loop
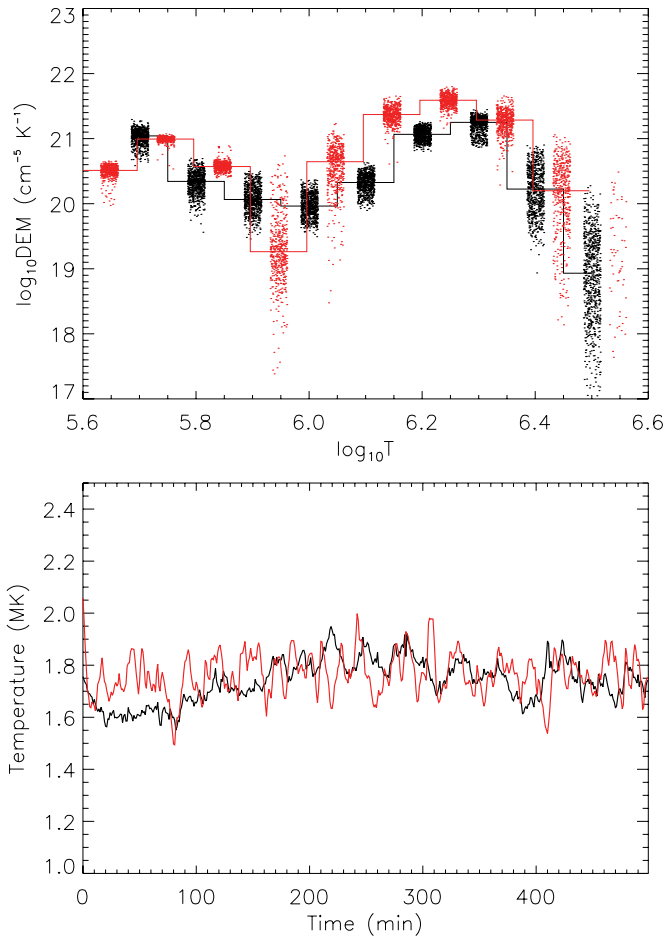
Figure 11. Same as Figure 7, but obtained for hybrid heating model (case 3).
(A color version of this figure is available in the online journal.)

(like the one originating from a small bipole in the quiet Sun), as compared to the warm loops in the hotter active region, has to be further examined.

The models presented in this work assume that the strands are heated uniformly over their entire length. Alternatively, the strand can be heated in a non-uniform manner with localized and concentrated heat sources. If the heating is concentrated at the loop footpoints, this may lead to the loss of equilibrium in the energy balancing terms, as the radiative losses in the coronal section dominate the downward conductive flux. This will trigger the runaway cooling due to strong radiative losses and a condensation is formed in the coronal loops (for example, Hood & Priest 1980; Müller et al. 2004). This is a well-studied phenomenon in the formation of solar prominences (Antiochos & Klimchuk 1991; Antiochos et al. 1999). Recently, based upon the observed properties of the hot and warm loops in active regions, Klimchuk et al. (2010) have argued that the high concentration of heating low in the corona and the steady or quasi-steady heating models (leading to thermal non-equilibrium) can be ruled out. However, Peter et al. (2012) claim that a steady supply of energy is required even in the events of condensation in the corona to keep the coronal pressure. They also suggested that thermal non-equilibrium can be a valuable tool in investigating the plasma dynamics and heat input in the regions where condensation forms.

The studies on the role and importance of the thermal non-equilibrium in the formation of condensation in the short quiet-Sun loops are not extensive. Müller et al. (2003, 2004)

discussed in detail the numerical simulations of condensation and catastrophic cooling of short TR 10 Mm loops and longer 100 Mm coronal loops, respectively. They considered heating that has exponential height dependence along the loop and further suggested that the catastrophic cooling is initiated by the loss of equilibrium at the loop apex due to concentration of heating at the footpoints, but not due to a drastic decrease of the total loop heating.

Note that the strands in a loop may interact in a very complex manner, and their response to the condensation is the key objective to be addressed. Further work is necessary to get a better picture of the nature and location of the heating, observational signatures of condensation, and finally the role of magnetic field in this whole process. A complete set of answers for these questions is still elusive and we need more observational constraints to narrow down the possibilities.

APPENDIX A

EBTEL AND LOOPS THAT EXPAND WITH TIME

The standard version of EBTEL assumes a symmetric loop with constant loop length and uniform cross-section. The model is based on the 1D time-dependent energy conservation equation:

$$\frac{\partial E}{\partial t} = -\frac{\partial}{\partial s} v(E + P) - \frac{\partial F_c}{\partial s} + Q - n^2 \Lambda(T), \qquad (A1)$$

where s is a spatial coordinate along the magnetic field; $E = (3/2)P + (1/2)\rho v^2$ is the total energy density; n, T, P, and v are the electron number density, temperature, total pressure, and plasma bulk velocity, respectively; F_c is the heat flux; Q is volumetric heating rate; and $\Lambda(T)$ is the radiative loss function for optically thin plasma. It is assumed that both the velocity and heat flux vanish at the loop apex due to symmetry. Also, the flow velocity is subsonic, and gravity is neglected in the energy equation. Integrating the above equation over the coronal (L) and TR (l) lengths with the above assumption, we obtain

$$\frac{3}{2}L\frac{\partial \bar{P}}{\partial t} \approx \frac{5}{2}P_0 v_0 + F_0 + L\bar{Q} - \mathcal{R}_c, \qquad (A2)$$

$$\frac{3}{2}l\frac{\partial \bar{P}_{tr}}{\partial t} \approx -\frac{5}{2}P_0 v_0 - F_0 + l\bar{Q}_{tr} - \mathcal{R}_{tr}, \qquad (A3)$$

where the overbar denotes the spatial averages of the quantities over respective sections of the loop, and subscript 0 denotes the values at the base of the corona; $\mathcal{R}_c$ and $\mathcal{R}_{tr}$ are the coronal and the TR radiative loss rates, respectively. Neglecting the terms involving l (for a thin TR), and together with ideal gas law,[7]

_____

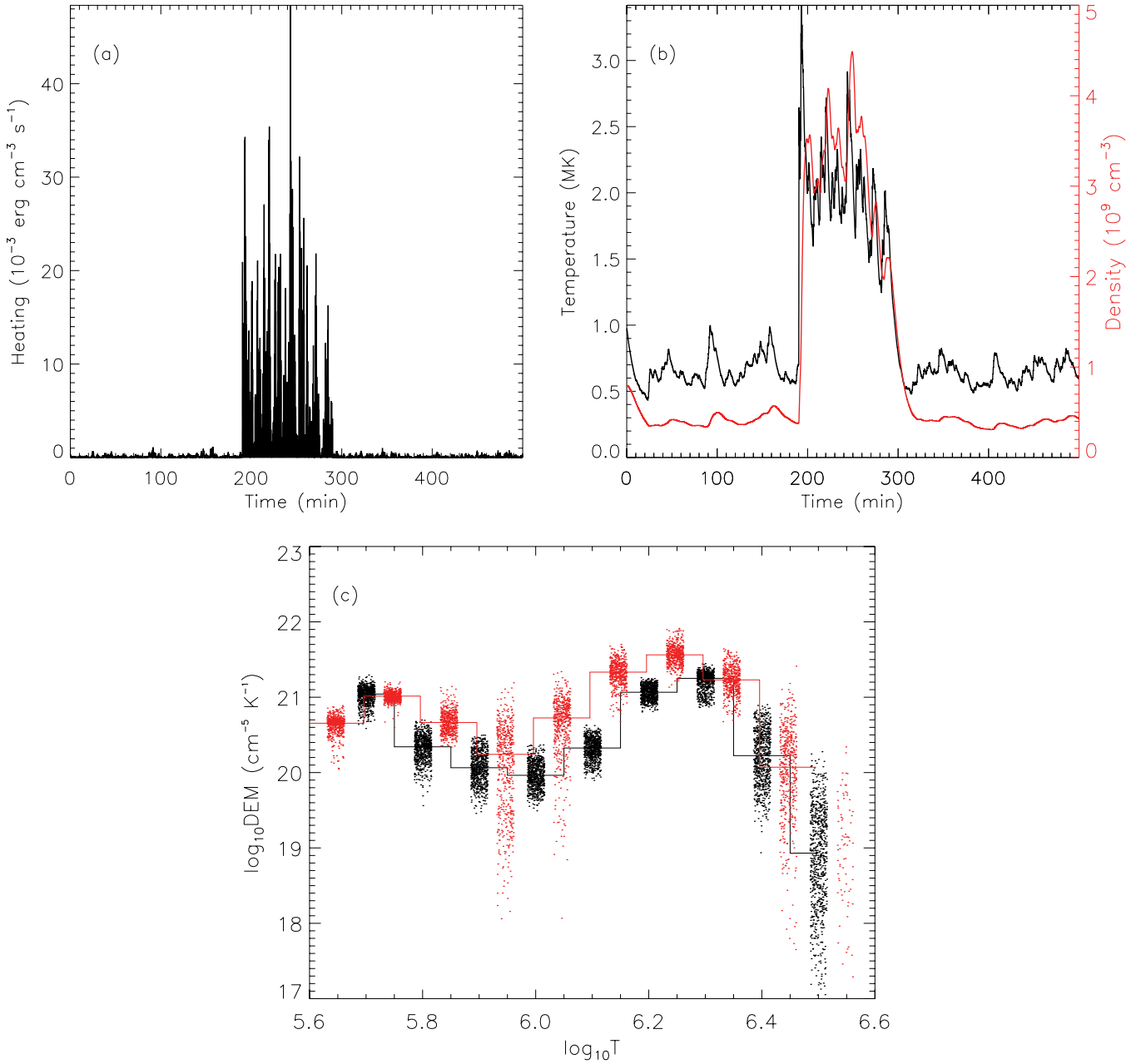[7] $P = 2nkT$, where k is Boltzmann's constant.

Figure 12. Alternative version of case 3 in which each strand receives high heating events 20% of its time, and low heating events the remaining time. (a) A sample heating profile is plotted. (b) Strand apex temperature (black, left axis) and strand density (red, right). (c) Same as the top panel of Figure 11.
(A color version of this figure is available in the online journal.)

$\bar{P}$ and $\bar{n}$ can be approximated[8] with

$$\frac{d\bar{P}}{dt} \approx \frac{2}{3}\left[\bar{Q} - \frac{1}{L}(\mathcal{R}_c + \mathcal{R}_{tr})\right], \quad\quad (A4)$$

$$\frac{d\bar{n}}{dt} \approx -\frac{1}{5kLT_0}(F_0 + \mathcal{R}_{tr}). \quad\quad (A5)$$

For a given heating rate $\bar{Q}(t)$, the EBTEL model returns $\bar{P}$, $\bar{n}$, and $\bar{T}$ with other useful quantities.

For a uniformly expanding strand of length $L(t)$ and radius $R(t)$ adiabatically, the above equations are modified by adding a term $-\gamma\bar{P}\xi(t)$ on the right-hand side of Equation (A4), and

$-\bar{n}\xi(t)$ in Equation (A5), where $\gamma = 5/3$ is the ratio of specific heats and

$$\xi(t) = \frac{1}{L}\frac{dL}{dt} + \frac{2}{R}\frac{dR}{dt}. \quad\quad (A6)$$

The strand pressure, density, and temperature are modeled accordingly. The time-varying length and radius of a single strand are shown as thin solid and dashed curves, respectively, in Figure 5. Note that $R(t)$ explicitly enters the scheme only through Equation (A6), and everywhere else it is absorbed due to volumetric averaging.

APPENDIX B

MODEL FOR LOOPS THAT EXPAND WITH HEIGHT

In this section we describe a loop model for the case that the cross-sectional area A varies along the loop. For simplicity, the

---

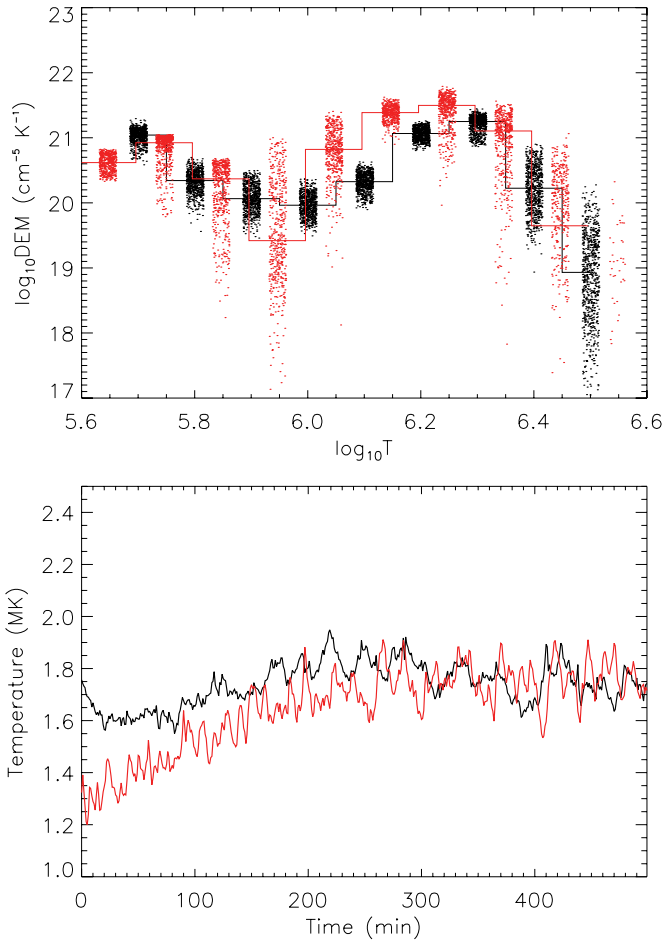[8] Simple volumetric averaging yields similar results.

Figure 13. Hybrid heating model with expanding length and radius as shown in Figure 5 (thin solid and dashed curves, respectively). Both the length and radius of the loop vary slowly with time. In this case the temperature (red, lower panel) increases as the length of the loop increases.

(A color version of this figure is available in the online journal.)

area $A(T)$ is considered to be a function of temperature:

$$A(T) = \exp\left\{\ln\gamma\left[\frac{z(T)}{z(T_{max})} - 1\right]\right\}, \qquad (B1)$$

where T_{max} is the maximum temperature at loop top and $z(T)$ is a monotonically increasing function, starting with $z \approx 0$ at the base of the TR. We use $z(T) = y + \sqrt{1 + y^2}$ with $y = (x - x_0)/x_1$ and $x = \log_{10} T$. The constants x_0 and x_1 are set to 6.0 and 0.2, respectively, so that most of the area change occurs near a temperature of 1 MK. Similarly, the volumetric heating rate is

$$Q(T) = Q_{max}\left(\frac{T}{T_{max}}\right)^m, \qquad (B2)$$

where Q_{max} is the heating rate at the loop top and m is an exponent (for the models presented here we set $m = 0$). The loop is assumed to be symmetric, and heating is assumed to be steady in time. We solve the following energy balance equation:

$$\frac{\partial}{\partial s}(A F_c) = A(T)\left[Q(T) - n^2\Lambda(T)\right], \qquad (B3)$$

where s is a spatial coordinate along the magnetic field, $F_c(s) \equiv -\kappa_0 T^{5/2}\partial T/\partial s$ is the conductive heat flux, $n(s)$ is the electron density, and $\Lambda(T)$ is the radiative loss function, which is taken from Klimchuk et al. (2008). Multiplying Equation (B3) by $A F_c$ and integrating over position along the loop, we obtain

$$\frac{1}{2}A^2 F_c^2 = \kappa_0 Q_{max}[f E_1(T) - E_2(T)], \qquad (B4)$$

where

$$E_1(T) = \int_{T_{base}}^{T} A^2(T)\Lambda(T)T^{1/2}dT, \qquad (B5)$$

$$E_2(T) = \int_{T_{base}}^{T} A^2(T)(T/T_{max})^m T^{5/2}dT. \qquad (B6)$$

Here, T_{base} is the temperature at the base of the TR ($T_{base} = 10^4$ K), and we assume $F_c = 0$ at the base. The factor f is given by

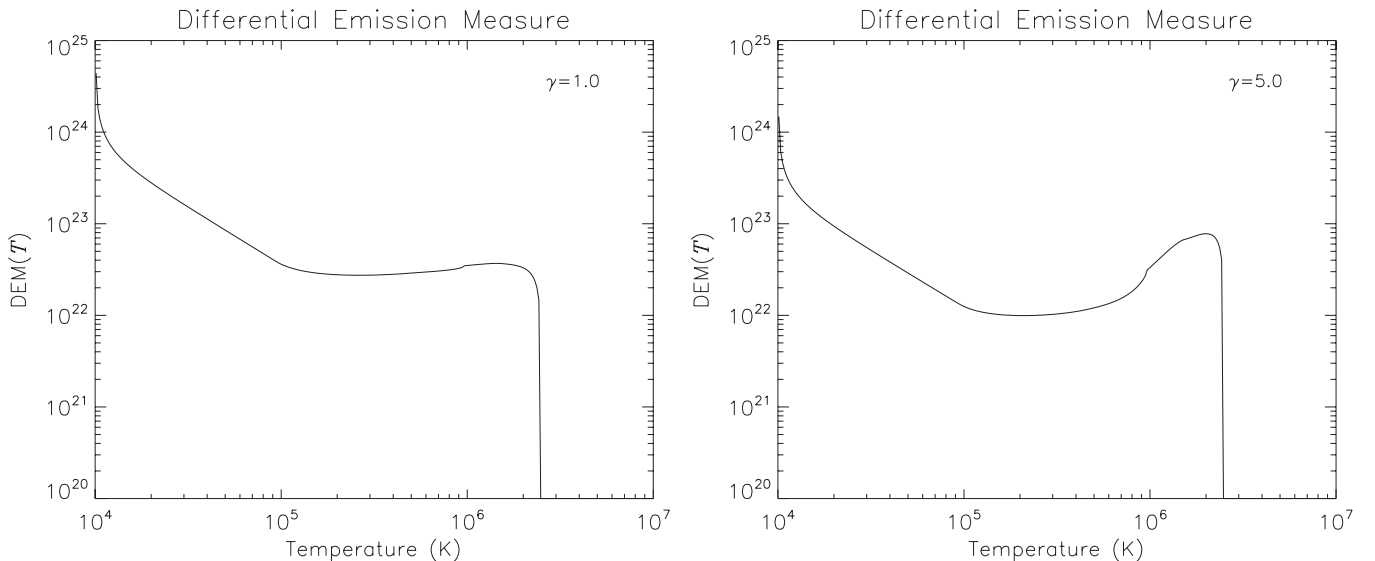$$f \equiv \frac{P^2}{4k^2 Q_{max}} = \frac{E_2(T_{max})}{E_1(T_{max})}, \qquad (B7)$$

Figure 14. Results from a simple loop model assuming steady heating. Left panel: DEM of a loop with expansion factor (γ) = 1. Note the flat DEM in the range of $10^5 < T(K) < 10^6$. Right panel: same as the left panel, but with $\gamma = 5$. The DEM now shows a clear peak at $T \approx 2$ MK.

where $P = 2nkT$ is the plasma pressure (a constant) and the last equality in (B7) follows from the requirement that $F_c = 0$ at the loop top. Then the loop half-length L is given by

$$L = \int_{s_{\text{base}}}^{s_{\text{max}}} ds = \left(\frac{\kappa_0}{2 Q_{\text{max}}} \right)^{1/2} \int_{T_{\text{base}}}^{T_{\text{max}}} \frac{A(T) T^{5/2} dT}{\sqrt{f E_1(T) - E_2(T)}}. \tag{B8}$$

For a given peak temperature T_{max} and half-length L, we can compute the heating rate Q_{max}, pressure P, heat flux $F_c(T)$, and density $n(T)$. Then the DEM is given by $\varphi(T) = n^2(T) A(T) (\partial T / \partial s)^{-1}$. Since the area factor is normalized such that $A(T_{\text{max}}) = 1$, this DEM(T) does not include the effects of a possible filling factor of the coronal loops.

REFERENCES

Alfvén, H. 1947, MNRAS, 107, 211
Antiochos, S. K., & Klimchuk, J. A. 1991, ApJ, 378, 372
Antiochos, S. K., MacNeice, P. J., Spicer, D. S., & Klimchuk, J. A. 1999, ApJ, 512, 985
Asgari-Targhi, M., & van Ballegooijen, A. A. 2012, ApJ, 746, 81
Cargill, P. J. 1994, ApJ, 422, 381
Cargill, P. J., Bradshaw, S. J., & Klimchuk, J. A. 2012, ApJ, 752, 161
Cargill, P. J., & Klimchuk, J. A. 1997, ApJ, 478, 799
Del Zanna, G., O'Dwyer, B., & Mason, H. E. 2011, A&A, 535, A46
Doschek, G. A., Landi, E., Warren, H. P., & Harra, L. K. 2010, ApJ, 710, 1806
Golub, L., Deluca, E. E., Sette, A., & Weber, M. 2004, in ASP Conf. Ser. 325, The Solar-B Mission and the Forefront of Solar Physics, ed. T. Sakurai & T. Sekii (San Francisco, CA: ASP), 217
Hood, A. W., & Priest, E. R. 1980, A&A, 87, 126
Klimchuk, J. A. 2006, SoPh, 234, 41
Klimchuk, J. A., Karpen, J. T., & Antiochos, S. K. 2010, ApJ, 714, 1239
Klimchuk, J. A., Patsourakos, S., & Cargill, P. J. 2008, ApJ, 682, 1351
Lemen, J. R., Title, A. M., Akin, D. J., et al. 2012, SoPh, 275, 17
Markwardt, C. B. 2009, in ASP Conf. Ser. 411, Astronomical Data Analysis Software and Systems XVIII, ed. D. A. Bohlender, D. Durand, & P. Dowler (San Francisco, CA: ASP), 251
Müller, D. A. N., Hansteen, V. H., & Peter, H. 2003, A&A, 411, 605
Müller, D. A. N., Peter, H., & Hansteen, V. H. 2004, A&A, 424, 289
Nakariakov, V. M., & Verwichte, E. 2005, LRSP, 2, 3
Narain, U., & Ulmschneider, P. 1996, SSRv, 75, 453
O'Dwyer, B., Del Zanna, G., Mason, H. E., Weber, M. A., & Tripathi, D. 2010, A&A, 521, A21
Parker, E. N. 1988, ApJ, 330, 474
Pérez-Suárez, D., Maclean, R. C., Doyle, J. G., & Madjarska, M. S. 2008, A&A, 492, 575
Pesnell, W. D., Thompson, B. J., & Chamberlin, P. C. 2012, SoPh, 275, 3
Peter, H., Bingert, S., & Kamio, S. 2012, A&A, 537, A152
Reale, F. 2010, LRSP, 7, 5
Rosner, R., Tucker, W. H., & Vaiana, G. S. 1978, ApJ, 220, 643
Scherrer, P. H., Schou, J., Bush, R. I., et al. 2012, SoPh, 275, 207
Schmelz, J. T., & Pathak, S. 2012, ApJ, 756, 126
Schou, J., Scherrer, P. H., Bush, R. I., et al. 2012, SoPh, 275, 229
Spadaro, D., Lanza, A. F., Lanzafame, A. C., et al. 2003, ApJ, 582, 486
Tripathi, D., Mason, H. E., & Klimchuk, J. A. 2010, ApJ, 723, 713
Ugarte-Urra, I., Doyle, J. G., & Del Zanna, G. 2005, A&A, 435, 1169
Ugarte-Urra, I., & Warren, H. P. 2012, ApJ, 761, 21
Ugarte-Urra, I., Warren, H. P., & Brooks, D. H. 2009, ApJ, 695, 642
Vaiana, G. S., Krieger, A. S., & Timothy, A. F. 1973, SoPh, 32, 81
Viall, N. M., & Klimchuk, J. A. 2012, ApJ, 753, 35
Warren, H. P., Winebarger, A. R., & Brooks, D. H. 2010, ApJ, 711, 228
Weber, M. A., Deluca, E. E., Golub, L., & Sette, A. L. 2004, in IAU Symp. 223, Multi-Wavelength Investigations of Solar Activity, ed. A. V. Stepanov, E. E. Benevolenskaya, & A. G. Kosovichev (Cambridge: Cambridge Univ. Press), 321
Winebarger, A. R., Schmelz, J. T., Warren, H. P., Saar, S. H., & Kashyap, V. L. 2011, ApJ, 740, 2
Zirker, J. B. 1993, SoPh, 148, 43